Geophysical Journal International

Geophys. J. Int. (2016) **206,** 792–806
Advance Access publication 2016 April 29
GJI Seismology

doi: 10.1093/gji/ggw173

Uncertainty estimations for moment tensor inversions: the issue of the 2012 May 20 Emilia earthquake

Laura Scognamiglio, Federica Magnoni, Elisa Tinti and Emanuele Casarotti

Istituto Nazionale di Geofisica e Vulcanologia, Roma, Italy. E-mail: laura.scognamiglio@ingv.it

Accepted 2016 April 26. Received 2016 April 26; in original form 2015 October 1

SUMMARY

Seismic moment tensor is one of the most important source parameters defining the earthquake dimension and style of the activated fault. Geoscientists ordinarily use moment tensor catalogues, however, few attempts have been done to assess possible impacts of moment magnitude uncertainties upon their analysis. The 2012 May 20 Emilia main shock is a representative event since it is defined in literature with a moment magnitude value (M_w) spanning between 5.63 and 6.12. A variability of ∼0.5 units in magnitude leads to a controversial knowledge of the real size of the event and reveals how the solutions could be poorly constrained. In this work, we investigate the stability of the moment tensor solution for this earthquake, studying the effect of five different 1-D velocity models, the number and the distribution of the stations used in the inversion procedure. We also introduce a 3-D velocity model to account for structural heterogeneity. We finally estimate the uncertainties associated to the computed focal planes and the obtained M_w. We conclude that our reliable source solutions provide a moment magnitude that ranges from 5.87, 1-D model, to 5.96, 3-D model, reducing the variability of the literature to ∼0.1. We endorse that the estimate of seismic moment from moment tensor solutions, as well as the estimate of the other kinematic source parameters, requires coming out with disclosed assumptions and explicit processing workflows. Finally and, probably more important, when moment tensor solution is used for secondary analyses it has to be combined with the same main boundary conditions (e.g. wave-velocity propagation model) to avoid conflicting results.

Key words: Time-series analysis; Inverse theory; Earthquake source observations; Wave propagation.

1 INTRODUCTION

The 2012 May 20 (02:03:50 UTC) Emilia earthquake is the main shock of a seismic sequence occurred in the Po Plain (Northern Italy) region between May and the end of 2012. After the main event, the sequence accounts for six earthquakes larger than magnitude M_L 5 and more than 3000 aftershocks. This sequence activated a fault system elongated for almost 50 km in the east–west direction and centred on the village of Mirandola, the epicentre of the main shock. From the geodynamical point of view, the Po Plain is in a context of active convergence. It is the foreland of two opposing verging fold-and-thrust belts: the Southern Alps to the north and the Northern Apennines to the south (Vannoli *et al*. 2015). This results in a remarkable tectonic diversity and heterogeneous crustal structure.

The moment magnitude, M_w, estimate of the 2012 May 20 Emilia event represents a peculiar case. Actually, in literature there are at least six seismic moment tensor solutions based on seismological data that use different wave speed models, stations, filter types or frequencies. The resulting M_w values span between 5.63 and 6.12 (Table 1). This range corresponds to a difference of 0.49 units in magnitude and to a factor of 5.4 in seismic moment release. As often occurs in the literature, all these solutions are reported without uncertainty analysis or, when the standard errors are available (for example in GCMT solutions), they are generally related to the inversion procedure. This means that since they do not include systematic effects due to the choice of velocity model or processing parameters, they underestimate the uncertainties (Valentine & Trampert 2012). However, estimating accurate earthquake source parameters and evaluating the corresponding uncertainties are important tasks in seismology. A proper characterization of earthquake magnitude and faulting style is fundamental to understand tectonics and earthquake dynamics. Moreover, an unambiguous M_w estimate is of primary importance when dealing with real time seismology since, for example, it is an input parameter for shakemap generation (Wald *et al*. 1999), for discriminating between tsunamigenic events (e.g. *NEAMTWS: Tsunami Early Warning*) and for short-term seismic hazard estimations (Werner & Sornette 2008). Errors in magnitude can also have a large, detrimental effect on operational earthquake forecasts (Marzocchi *et al*. 2014) whose statistical models depend on the correct parametrization of the seismicity. A lack of uncertainty associated to M_w estimate or partial information of assumed framework (e.g. wave propagation model undisclosed or unpublished) could be critical for the inference of other seismological

Table 1. Moment tensor solutions based on seismological data calculated for the 2012 May 20 Emilia main shock. For each solution we report M_w, seismic moment M_0, strike, dip, rake, depth, the used velocity model, the analysed frequency band and the reference.

	M_w	M_0 (dyne cm)	Strike (°)	Dip (°)	Rake (°)	Depth (km)	Velocity model	Frequency band (Hz)	Author
1.	5.83	7.00E+24	280/103	44/46	88/92	5.0	CIA	0.02–0.05	Scognamiglio *et al*. (2012)
2.	5.63	3.47E+24	285	45	90	7.0	PADANIA	0.01–0.04	Malagnini *et al*. (2012)
3.	6.03	1.37E+25	282/97	51/39	93/86	6.0	VENE-PLAIN	0.01–0.05	Saraò & Peruzza (2012)
4.	6.11	1.81E+25	279/109	60/30	85/99	11.4	see Pondrelli *et al*. (2011)	0.0167–0.0286	Pondrelli *et al*. (2012)
5.	6.12	1.89E+25	286/103	65/25	91/87	7.0	IASP91	0.01–0.05	Cesca *et al*. (2013)
6.	6.10	1.74E+25	304/88	61/35	109/60	12.0	PREM	see Ekström *et al*. (2012)	GCMT

parameters, suggesting caution for seismic hazard assessment, coulomb stress transfer determination and other analyses where self-consistency is important. This is just what arose in the scientific debate after the 2012 Emilia main shock about the applicability of the Italian seismic hazard model (MPS04: http://zonesismiche.mi.ingv.it, and Stucchi *et al*. 2011). The large differences between the published moment magnitude solutions caused controversial results to reconstruct hazard scenarios in this area (Malagnini *et al*. 2012; Meletti *et al*. 2012).

Even though a systematic difference of ∼0.1/0.2 units in magnitude for the same event has been already observed between different catalogues (e.g. Kubo *et al*. 2002; Scognamiglio *et al*. 2009; Gasperini *et al*. 2012), still few efforts have been spent to quantify and identify the origin of the M_w's uncertainties. Moreover, during the first hours after an earthquake, the attention of the non-scientific community is focused on magnitude, and often M_w is perceived as an absolute and perpetual value so that discrepancy or evolution of this parameter leads to misunderstanding and debates (La Longa *et al*. 2014).

It is thus important to emphasize that earthquake moment tensor source parameters and their stability are critically dependent on three main elements: the assumed velocity structure of the Earth, the modelling approach and the data coverage, as reported in numerous studies (e.g. Kubo *et al*. 2002; Šílený 2004; Hjörleifsdóttir & Ekström 2010; Valentine & Trampert 2012). Many of these works suggest that the effect of the velocity model prevails upon the others. Moreover, it has been demonstrated the existence of a trade-off between source and structure and the theoretical reason of it (e.g. Pavlis & Booker 1980; Morelli & Dziewonski 1991; Valentine & Woodhouse 2010). However, quantitatively map this trade-off for any particular case is not trivial.

In literature, moment tensor solutions are retrieved by using 1-D or 3-D local, regional or global wave speed models. The choice mainly depends on the event's magnitude, on the inverted frequencies, on the epicentral distance of selected stations, and on the need of releasing real time solutions. In some areas and for some frequency ranges 1-D models could be adequate to reproduce the velocity structure for moment tensor inversions. Nevertheless, good 3-D models provide useful information for source parameter calculation, but they do not always exist or could not improve 1-D moment tensor solutions.

In this work, we deal with regionally computed moment tensor for a moderate magnitude earthquake, where the inverted stations have epicentral distances within ∼200 km. Being aware that the studied earthquake occurred in a tectonically complicated area, we want to understand the relative significance of known inaccuracies and their effect on the moment tensor parameters. We conduct a detailed analysis on the variability of moment tensor solution obtained for the main shock of the 2012 Emilia sequence due to the effect of the employed wave speed models (1-D and 3-D), the adopted inversion procedures, the number and azimuthal distribution of the considered stations, with the goal of providing more reliable estimates of the source parameters (strike, dip, rake and M_w) and corresponding uncertainties. The two adopted inversion methodologies are: Time Domain Moment Tensor (TDMT) technique (Dreger & Helmberger 1993) and Centroid Moment Tensor procedure based on 3-D wave speed models (CMT3D, Liu *et al*. 2004, Sections 2.1 and 4.1, respectively). We finally demonstrate that the moment tensor of the 2012 May 20 Emilia earthquake can be estimated with an acceptable uncertainty, mainly affected by the capability of the adopted velocity model to reproduce the regional crustal structure.

2 MOMENT TENSOR INVERSIONS IN 1-D STRUCTURES

To explore the effect of velocity model on moment tensor estimation, we compute TDMT solutions by fitting velocity waveforms of broad-band stations with synthetic waveforms derived from five different 1-D wave speed models. Data and synthetics are both filtered between 0.01 and 0.05 Hz. The use of an identical data set and data processing allows us to directly compare inversion results based only on the adopted velocity model without bias due to the different modelling approach.

2.1 Method

We follow the full-waveform TDMT technique originally proposed by Dreger & Helmberger (1993) and implemented at INGV by Scognamiglio *et al*. (2009). Starting from a given hypocentral location, the algorithm inverts local to regional three component broad-band velocity waveforms to estimate moment tensor in a point-source approximation. Seismic moment tensor is decomposed into the scalar seismic moment, a double-couple moment tensor (DC) and a compensated linear vector dipole moment tensor (CLVD). The isotropic component is constrained to be zero. Synthetic seismograms are represented as linear combination of eight fundamental Green's functions that form the basis functions for any arbitrarily oriented DC mechanism (for further details see Scognamiglio *et al*. 2009).

In this study, the Green's functions are computed by using the frequency-wavenumber integration code (FKPROG) of Saikia (1994) for three layered, regionally calibrated velocity structures: CIA (Herrmann *et al*. 2011), PADANIA (Malagnini *et al*. 2012), VENETIAN PLAIN (Vuan *et al*. 2011), and two global models: PREM (Dziewonski & Anderson 1981) and IASP91 (Kennett & Engdahl 1991; Fig. 1a). We choose these 1-D profiles because they are those used in literature to compute the moment tensor of the Emilia sequence main shock (solutions in Table 1). The first model, CIA, has been obtained by integrating deep seismic reflection crustal profiles, surface wave dispersion and teleseismic *P*-wave receiver functions in Central Apennine. PADANIA model has been constructed by starting from the deeper part of CIA model

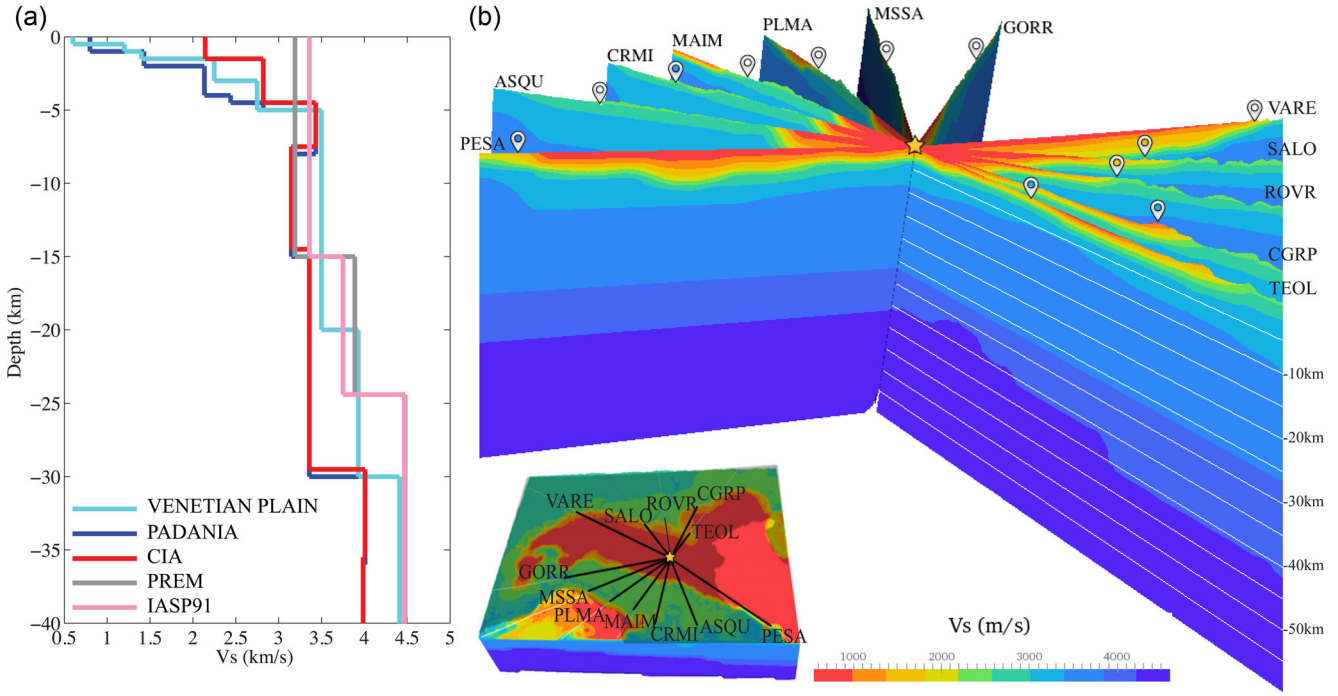

Figure 1. 1-D and 3-D tested wave speed models. (a) Red curve is for CIA model, cyan curve is for VENETIAN PLAIN model, blue curve is for PADANIA model, grey curve is for PREM model and pink curve is for IASP91. (b) 3-D MAMBo velocity model and the 12 selected stations.

and adding shallow low-velocity layers based on geological data and seismic profiles for the Po Plain. Finally, VENETIAN PLAIN velocity model has been mainly based on geophysical information from oil exploration. We also decide to test two global velocity models, PREM and IASP91, to verify if the higher published M_w values are due to a less calibrated wave speed structure.

Quality and reliability of moment tensor solutions are determined by the goodness of fit between synthetic and observed waveforms, which is quantified through the variance reduction (VR) parameter,

$$VR = \sum_i w_i \left(1 - \frac{\int [x_i(t) - d_i(t)]^2}{\int d_i{}^2(t)\,\mathrm{d}t}\right) 100\%, \quad (1)$$

where i is the station index, $x_i(t)$ the synthetic waveform, $d_i(t)$ the recorded waveform, and w_i is the inverse epicentral distance weight, that is more distant stations have a larger weight. For any fixed depth, the TDMT procedure attempts to find the best fit by cross-correlating the data with the synthetics and maximizing VR that represents an L2-like norm. Consequently, VR can be used as a tool to compare and quantify the quality of the solutions even adopting different methodologies, as we will show later in this study (Sections 3.1 and 5.1).

2.2 Data set and processing

We use velocity waveforms from broad-band three component stations provided by the Italian National Seismic Network (IV), the Regional Seismic Network of Northwestern Italy (GU) and the northeast Italy Broad-band Network (NI).

Data are extracted in 500 s windows starting 90 s before the event origin time, checked for signal-to-noise ratio larger than 5, corrected for instrument response and the horizontal components are rotated to great circle path. Finally, data and Green's functions are filtered by applying a low-pass filter followed by a high-pass filter in the frequency band 0.01–0.05 Hz characterized by 3-poles and 1-pass.

To examine the influence of velocity models (Section 3.1) we use data of 12 stations (red triangles in Fig. 2a). Among all the stations available soon after the earthquake occurrence, these 12 have been selected because they satisfy two important requirements: (i) being evenly distributed around the epicentre to assure good azimuthal coverage of not saturated stations and (ii) being close to the epicentral area to capture the effect of the local velocity structure. Then, to study the impact of station selection and distribution on the moment tensor variability we extend the data set to 75 stations (Sections 3.2 and 3.3).

3 TDMT RESULTS

Starting from the INGV hypocentral location (latitude 44.90°; longitude 11.26°; depth 10 km) and using waveforms coming from the 12 stations in Fig. 2(a) (red triangles), we compute the Emilia main shock moment tensor for the five 1-D velocity models (Table 2). To obtain the best result and maximize the cross-correlation for each velocity model, we perform a grid-search on the depth (Fig. 2b) and allow a limited time-shift of each synthetic waveform with respect to observed data. This shift is forced to be the same for the three station components. In this figure it is possible to appreciate the tendency of depth versus magnitude and the resulting variance reduction. We choose as moment tensor solution and centroid depth for each case those with the highest VR. The regional 1-D models come out with a similar preferred depth (5–6 km) but quite different M_w values, while the global models show a lower centroid depth (3 km) and the highest M_w values. The resulting beachballs are shown in Figs 2(c)–(g) and in Table 2.

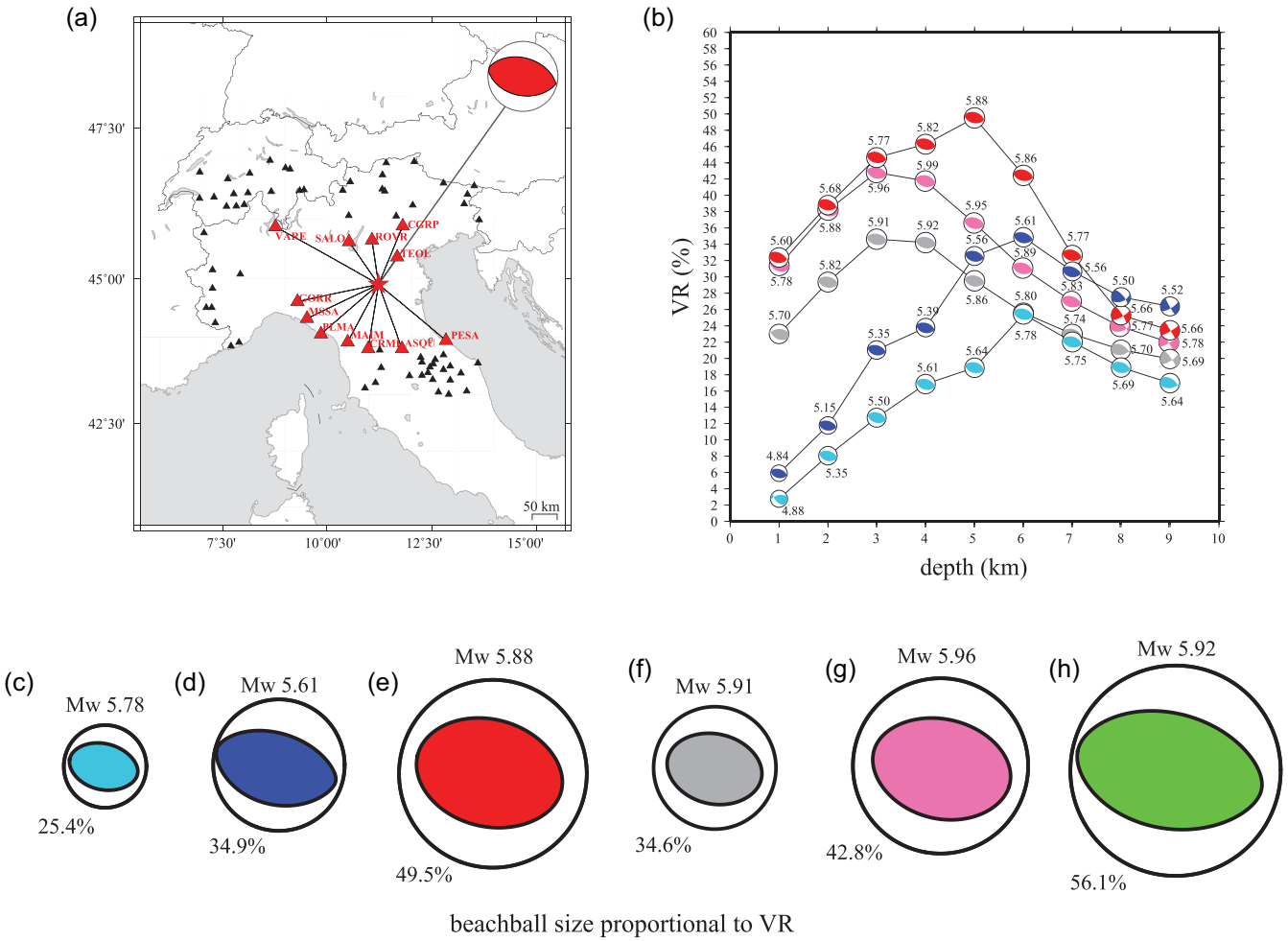

Figure 2. (a) Map with the 75 broad-band stations available for the study; red triangles represent the 12 stations selected for the first analysis of moment tensor inversions. (b) Variation of M_w and VR as a function of depth for the five considered 1-D wave speed models. Colours are the same as in Fig. 1(a). (c)–(h) Focal mechanisms resulting from the performed tests. (c)–(g) are for the 1-D models in Fig. 1(a), while green mechanism (h) comes from the 3-D MAMBo velocity model (Fig. 1b). The numbers on the top of beachballs indicate the computed M_w, while the numbers at the bottom are the resulting VR. The dimension of the ball is proportional to the VR value.

Table 2. The table summarizes the moment tensor source parameters obtained by using TDMT procedure with the five 1-D wave speed models tested in our paper, and CMT3D procedure with the 3-D MAMBo model, always inverting the same 12 selected stations. For each velocity model we report: moment magnitude M_w, seismic moment M_0, strike, dip, rake, depth, variance reduction VR and double couple percentage DC.

Models	M_w	M_0 (dyne cm)	Strike (°)	Dip (°)	Rake (°)	Depth (km)	VR (%)	DC (%)
1. CIA	5.88	8.11E+24	288/100	45/45	95/85	5	49.5	67
2. PADANIA	5.61	3.28E+24	289/100	51/39	95/83	6	34.9	97
3. VENE-PLAIN	5.78	5.88E+24	286/102	47/43	93/87	6	25.4	65
4. PREM	5.91	9.27E+24	282/102	47/43	90/90	3	34.6	65
5. IASP91	5.96	1.10E+25	282/105	48/42	88/93	3	42.8	70
6. MAMBo	5.92	9.44E+24	288/96	46/44	98/82	5	56.1	–

3.1 Velocity model effect

Comparing the moment tensor results obtained with the five tested velocity models (Figs 2c–g), we find that VR values range between 25.4 and 49.5 per cent, while M_w values between 5.61 and 5.96.

The worst-fitting solution is obtained with VENETIAN PLAIN and has $M_w = 5.78$, VR = 25.4 per cent and DC = 65 per cent. Solutions with VR < 30 per cent have moment tensor parameters not completely trustworthy due to a poor fit between data and synthetics as demonstrated in Fig. 3 (cyan waves). The model does a sufficient job fitting the main body wave pulses, especially if we consider the closest stations: TEOL, ROVR and SALO. On the contrary, it introduces complexities not existing in the real data in the later arrivals of many horizontal components.

The generation of unrealistic arriving pulses in synthetic seismograms can be observed in the waveforms computed with PADANIA model as well (Fig. 3, blue waves). This is clearly evident in the tangential components of ROVR, SALO, MSSA and GORR. As a consequence of the poor fit, the moment tensor solution obtained with this model results in a still low variance reduction, VR = 34.9 per cent. On the contrary, the kinematic parameters are reasonably constrained as shown by the resulting high double

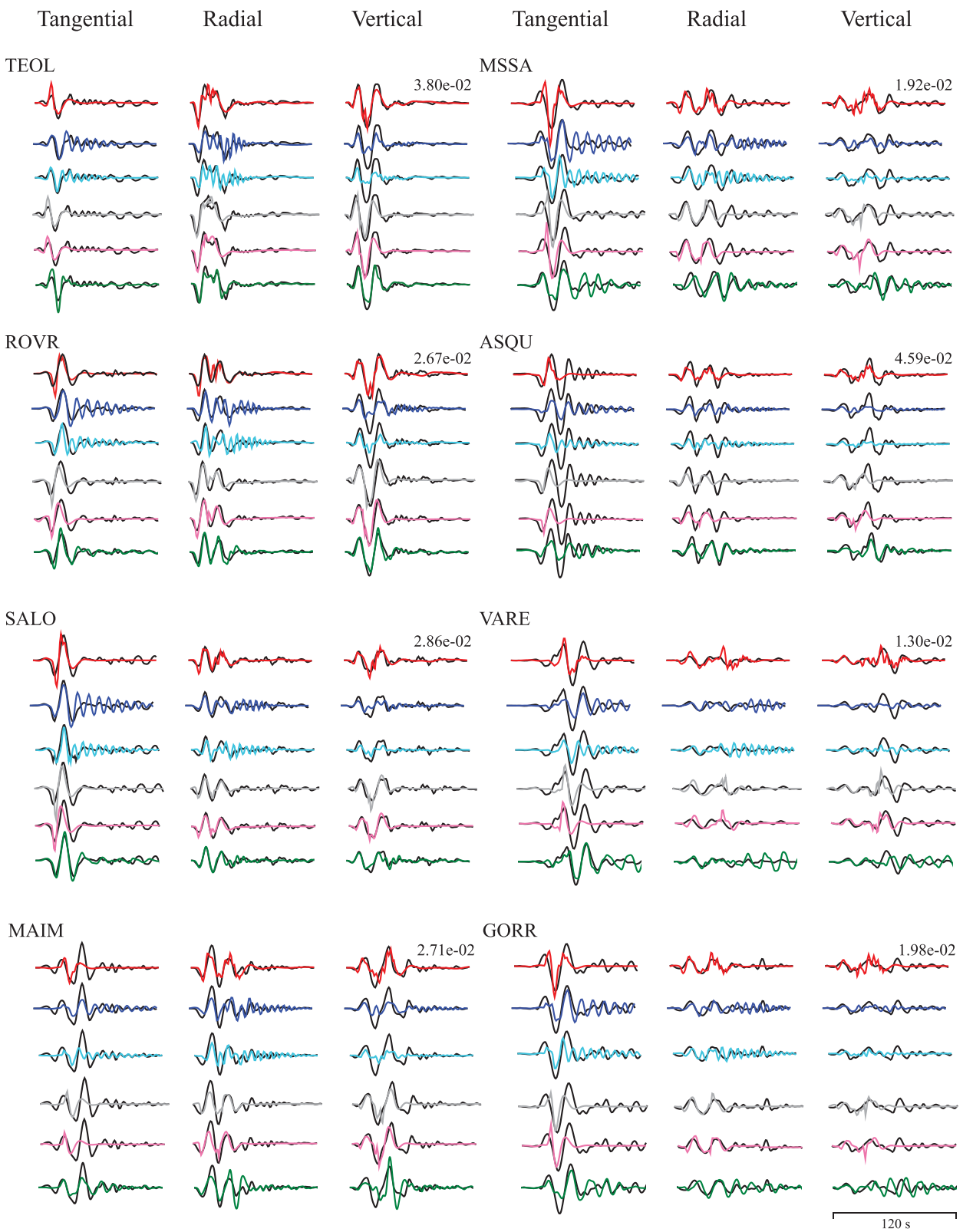

Figure 3. Waveform comparison between real data (black curves) and synthetics for 8 representative stations obtained with: CIA (red), PADANIA (blue), VENETIAN PLAIN (cyan), PREM (grey), IASP91 (pink) and 3-D MAMBo (green) velocity models. These solutions are obtained for the frequency range 0.01–0.05 Hz, and high-pass and low-pass filters with 3-poles and 1-pass. Waveforms for each station are normalized to the maximal value over the components. This value (in seconds) is on the right-hand side of each station's group.

couple, DC = 97 per cent. The moment magnitude is 5.61, the lower edge of the obtained magnitude interval.

Inverting with 1-D CIA model we get VR = 49.5 per cent, DC = 67 per cent and M_w = 5.88. Looking at the waveforms' fit (Fig. 3, red waves), CIA model is capable to reproduce the main waveform pulses on all the three components both in amplitude and in phase, and it does not generate the reverberation in synthetic waveforms coming from sedimentary layers of the other two tested velocity models. Therefore, based on the goodness of fit between data and synthetics, CIA model produces a better solution than the PADANIA or VENETIAN PLAIN models.

The last tested velocity models are PREM and IASP91. PREM gives a MT solution characterized by VR = 34.6 per cent, DC = 65 per cent and M_w = 5.91, while IASP91 MT best solution has VR = 42.8 per cent, DC = 80 per cent and M_w = 5.96. These global Earth models reproduce the amplitude of the main body waves and do not generate fake later arrivals, but are too fast to allow a good time alignment between real and synthetic phases.

The resulting values of the source parameters for the five solutions are reported in Table 2.

The analysis we performed on the wave speed models reveals that 1-D CIA model should be preferred with respect to the other two tested regional models when dealing with moment tensor solution of the Emilia main shock. This result could be unexpected, because CIA lacks the shallow sedimentary layers that characterize the geological structure of the Pianura Padana basin at the source location (Malagnini *et al*. 2012; Molinari *et al*. 2015). However, since observed waveforms have no reverberations, we can state that sediment layers are not significant for the analysed frequency band, the dimension of source and stations' distances higher than 60 km. In view of these results, in the following analyses we will only use CIA model.

Besides, the moment tensor solutions obtained with global velocity models do not completely explain the high moment magnitude values found in literature, contrary to what we expected. The values in literature are probably due to a combination of such global models with the adopted filter, frequencies and stations.

By using the same method, the same data set and processing, we reduce the M_w variability in the present literature from 0.49 to 0.35 (see solutions 1–5 in Table 2). This is the difference effectively coming from the velocity model.

3.2 Station selection effect

Because of the complexity of the studied area, we decide to investigate in more detail the variability of the source parameters depending on the station selection. Using only the 1-D CIA model, we enlarge the data set of available stations to 75 (all the triangles in Fig. 2a).

First of all, we perform a bootstrap analysis with 500 MT inversions obtained by randomly selecting 12 stations out of the 75. The empty red histograms in Fig. 4 represent the distributions of the obtained source parameters and the variance reduction for all the 500 1-D CIA solutions, while the solid red histograms are referred to the solutions with VR > 30 per cent, where 30 per cent is our threshold for reliable solutions when inverting more than eight stations (http://cnt.rm.ingv.it/en/help#TDMT).

The bootstrap analysis results in quite narrow source parameter distributions. The inferred median M_w value is 5.87 and the associated uncertainty is [5.81–5.92] (solid and dotted red lines in Fig. 4, respectively. This uncertainty is expressed as a confidence interval at 95 per cent that represents the range of plausible values of the parameter due to the sampling of the given model (Table 3).

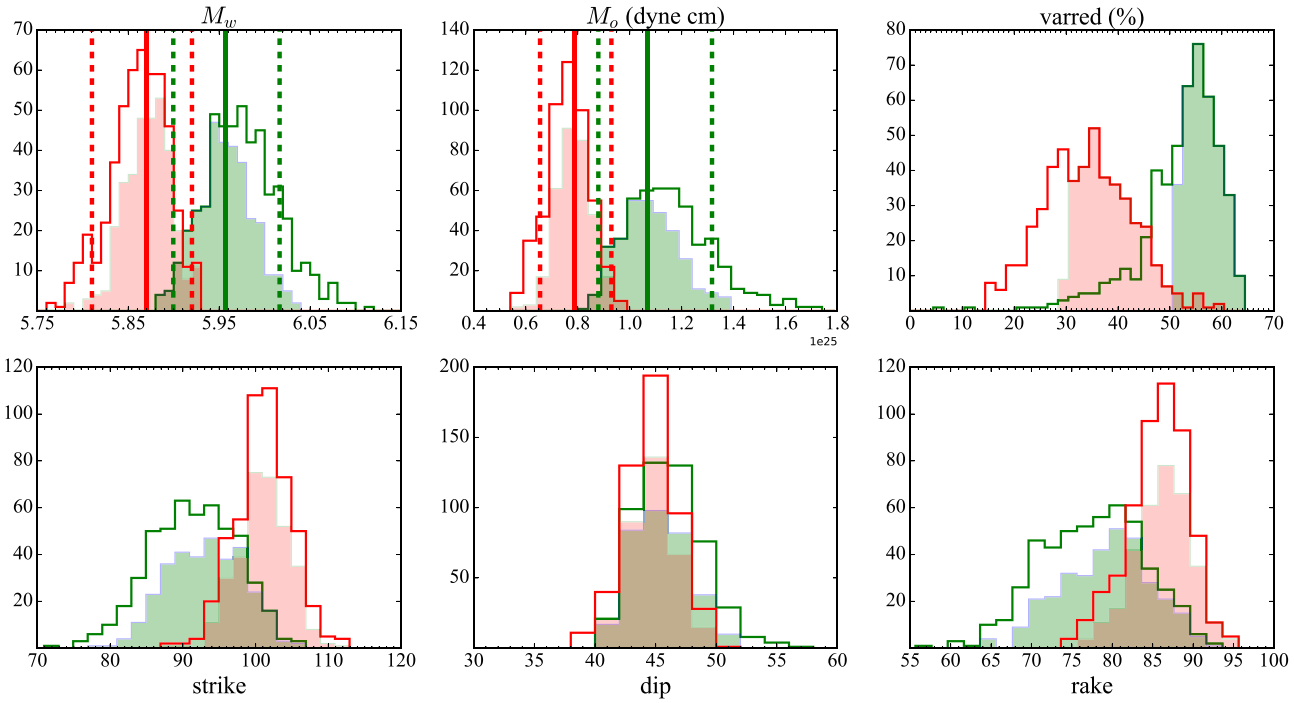

Figure 4. Results from the bootstrap analysis with 12 randomly chosen stations. Empty histograms represent the source parameters resulting from all the 500 MT solutions, red is for 1-D inversion with CIA velocity model, while green is for 3-D inversion with MAMBo model. Solid red histograms are the 329 1-D MT solutions with VR > 30 per cent. Solid green histograms are the best 329 MT solutions obtained with 3-D model. Solid and dotted lines in M_w and M_0 panels are the median values and the limits of the confidence interval at 95 per cent for the best 329 solutions, respectively. For M_w these values are: 5.87 and [5.81–5.92] for the 1-D CIA case; 5.96 and [5.90–6.02] for the 3-D MAMBo case.

Table 3. The table summarizes the moment tensor source parameters obtained from the bootstrap analysis with the 1-D CIA and the 3-D MAMBo models. The parameters are: moment magnitude M_w, seismic moment M_0, strike, dip and rake and depth. Note that for M_w and M_0 the reported values are the medians calculated for the distributions of the best 329 MT solutions in the two cases and the uncertainties are the corresponding confidence intervals at 95 per cent. Instead, for strike, dip and rake the values and uncertainties of both 1-D and 3-D cases are the geometric medians and confidence intervals at 95 per cent obtained from the multivariate analysis (see Section 6).

Models	M_w	M_w uncertainty	M_o (dyne cm)	M_0 uncertainty (dyne cm)	Strike (°)	Strike uncertainty (°)	Dip (°)	Dip uncertainty (°)	Rake (°)	Rake uncertainty (°)	Depth (km)
CIA	5.87	5.81–5.92	7.86E+24	(6.55–9.30)E+24	101	94–107	44	41–48	87	79–93	5
MAMBo	5.96	5.90–6.02	10.70E+24	(8.80–13.17)E+24	93	84–102	45	41–50	79	69–89	5

Regarding strike, dip and rake, instead, the solution for these parameters and related uncertainty cannot be the medians and confidence intervals from the histograms, but should be deduced by looking at the variability of the focal mechanism for the given model, because they are not independent parameters. A detailed study about it is thus reported in Section 6, also in comparison with 3-D case. It is noteworthy that while the solid histograms of strike, dip and rake parameters show the same features of the corresponding empty histograms, the solid histogram of M_w (and M_0) excludes the lower values documented in the empty histogram. We repeat the same tests with different values of the VR threshold (up to 40 per cent) obtaining similar results.

We found that the median values of M_w and M_0 take place close to the moment tensor solution previously presented in Section 3.1 using 1-D CIA model, hereinafter TDMT+1DCIA solution ($M_w = 5.88$, see also solution 1 in Table 2). This outcome suggests that 12 well-distributed stations are enough to explore the model variability and catch the moment tensor characteristics.

We also see that the VR value of TDMT+1DCIA solution (49.5 per cent) lies among the highest values of the bootstrap distribution. This justifies the choice of the specific stations and highlights that a quite homogenous azimuthal coverage of the stations is required to get good solutions when a reliable 1-D model is used for the inversion. We will deeply deal with the azimuth effect in the next paragraph.

To better study the reliability and variability of source solution due to station selection, we perform new bootstrap analyses increasing the number of randomly selected stations for each inversion (see Figs S1 and S2 in the supporting information obtained with 24 and 36 stations, respectively). Increasing the number of stations, the distributions become narrower around median values that remain pretty stable. This result is expected because increasing the number of inverted stations we reduce the weight of poorly fitted stations and therefore the weight of not well represented heterogeneity of the real structure. We can thus state that, for the studied earthquake, using 12 stations in multiple inversions is sufficient and significant to get reliable moment tensor solutions and their related uncertainty. Indeed, in this way, we provide a more detailed sampling of the wave speed heterogeneities and we allow for a better exploration of the source parameter variability due to the structure model. For this reason in the following analyses we focus only on the distributions obtained with 12 stations. Notably, this bootstrap analysis gives an uncertainty in magnitude estimation (0.11) lower than the variability (0.35) due to the assumed velocity structure as previously discussed.

3.3 Stations distribution effect

We study the effect of the azimuthal distribution of the seismic stations on the variability of source parameters by calculating the moment tensor solution only with the stations, among the considered 75, located in each azimuth range of 60° starting from 0° and shifting by 30° each time (Fig. 5a).

For the inversions performed using 1-D CIA model, the resulting moment magnitude ranges between 5.77 and 5.93, with VR in the interval [15.3–70.0 per cent]. The lowest variance reduction values are obtained for sectors containing stations located in Northern Apennines. This highlights that for such a complex crustal structure a 1-D model can result inadequate for given azimuths. The M_w variability due to the azimuth is 0.16. The extreme M_w values have both good VR, leaving to the seismologist the discretion of choosing the most representative solution. This confirms that solutions obtained with large azimuthal gaps could only contain limited features of structure and source, as much as the velocity model diverges from the real crustal structure. Thus, performing a good azimuthal station selection is important in moment tensor computation with laterally homogeneous velocity structures. This analysis leads us to attempt a 3-D heterogeneous wave speed model to estimate a moment tensor solution that better accounts for the effect of structural complexities of the region.

4 CENTROID MOMENT TENSOR IN 3-D STRUCTURES

Given the results in previous sections, we decide to study the effect on moment tensor solution due to the use of a local wave speed model that includes 3-D heterogeneities.

Then, we analyse the obtained results in comparison with those for the 1-D CIA model.

4.1 Method

The point-source inversion method that we use with the 3-D wave speed model is the procedure presented by Liu *et al*. (2004) and implemented as a code for Centroid Moment Tensor in 3-D structures, namely CMT3D (see also Magnoni 2012). This technique allows one to invert for CMT by numerically calculating the Fréchet derivatives with respect to the considered source parameters and then minimizing the misfit between data and synthetics. This inversion procedure is based on three component full waveforms and can handle synthetic wavefield calculated for complex 3-D wave speed models. An initial moment tensor solution is used, in combination with a velocity model to numerically simulate both the initial synthetics and the synthetics required to construct the Fréchet derivatives (Liu *et al*. 2004). Then, a limited time-shift of each synthetic trace is allowed to maximize the cross-correlation with corresponding data in order to accommodate additional heterogeneity not included in the wave speed models. This shift can be different for each station's component, unlike TDMT procedure.

In this study, we simulate the initial synthetics and the six Fréchet derivatives using the spectral-element code

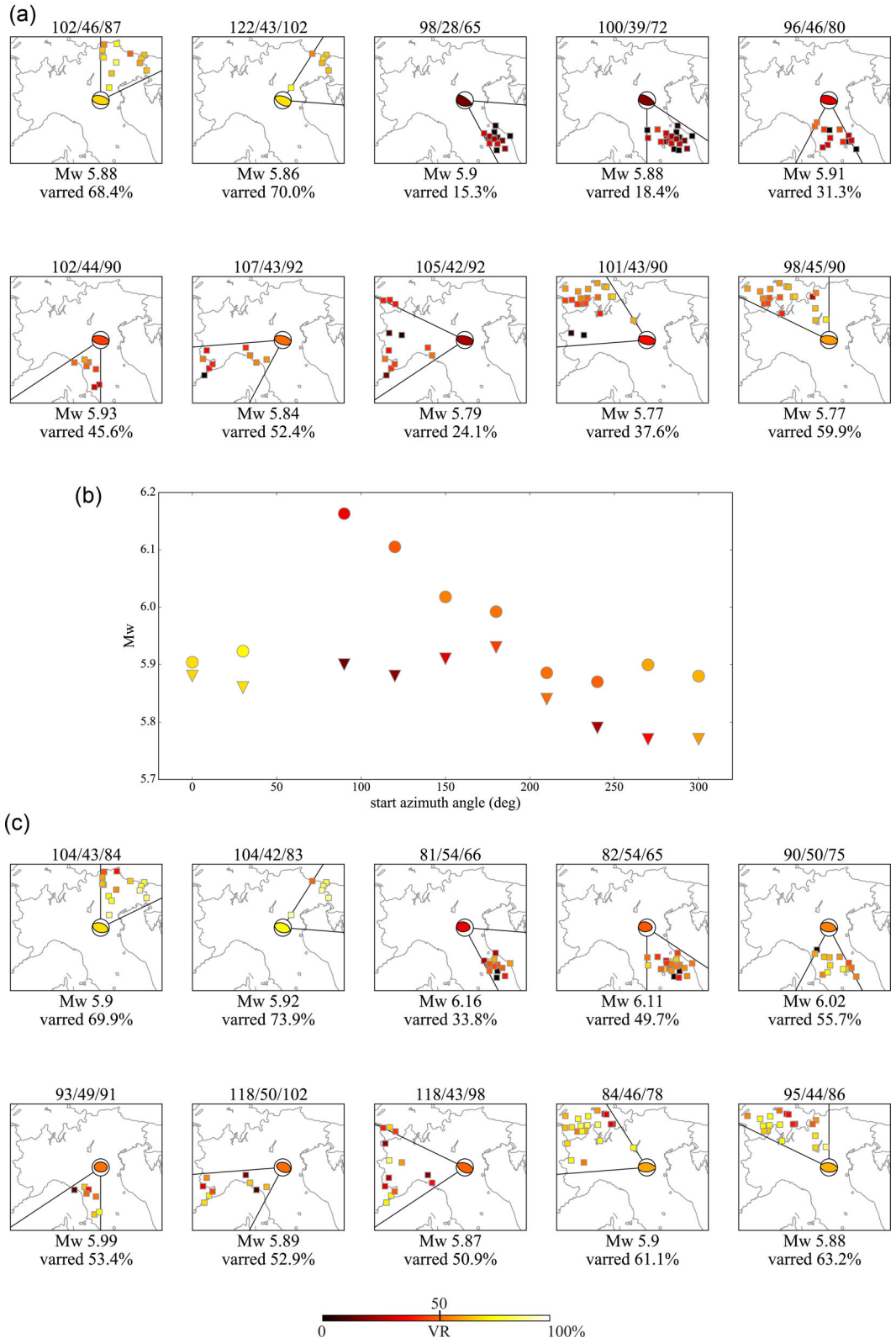

Figure 5. MT solutions of the 2012 May 20, Emilia main shock as a function of the azimuthal distribution of the stations obtained from the inversions with (a) the 1-D CIA model and (c) the 3-D MAMBo model. Each subpanel in both figures (a) and (c) represents the MT solution for the stations located within an azimuth range of 60°, starting from 0° in the top left subpanel and shifting the starting angle of 30° in each following subpanel. Note that the solution for the azimuth range 60°–120° has not been represented since there are no stations in this sector. The colour of the resulting beachballs corresponds to the VR of the solution, while the colour of the squares represents the VR of the single station (scale is at the bottom). The numbers on the top of each subpanel are strike/dip/rake of the preferred fault plane. Panel (b) shows the M_w values as a function of the starting azimuth angle for the 1-D case (coloured triangles) and the 3-D case (coloured circles). Colours of both triangles and circles refer to the VR of the corresponding solution.

SPECFEM3D_Cartesian (Peter *et al*. 2011) that allows for highly accurate full-waveform simulations also in very complex heterogeneous media. The initial source input for the simulations is given by the best TDMT solution, that is the one with 1-D CIA model (Table 2), while the adopted structure is described by a 3-D wave speed model for Northern Italy, MAMBo, developed by Molinari *et al*. (2015; Fig. 1b). This model has been derived from geological and seismological information and includes the main foredeep basin (Pliocene and Eocene) sediment layers that, in this region, can reach 8 km of depth. A zero-trace constraint is always imposed in the inversion. Although CMT3D allows for inversions of both location and MT, we decide to invert only for the 6 moment tensor components to be consistent with the TDMT procedure. The synthetics for the obtained solution are constructed by the code CMT3D as a linear combination of the calculated Fréchet derivatives (for the details see https://github.com/QuLogic/GRD_CMT3D).

Finally, to quantify the quality of the solution and compare the results to those obtained with the 1-D model, we calculate the variance reduction VR as defined in eq. (1).

4.2 Data set and processing

We initially consider velocity waveforms recorded by the 12 broadband three-component stations presented in Section 2.2 (red triangles in Fig. 2a), and then we enlarge the data set to the 75 stations for the bootstrap analysis (Sections 5.2, 5.3). The same processing described in Section 2.2 is applied to the data, the initial synthetic traces and those simulated to construct the Fréchet derivatives. We use the code FLEXWIN (Maggi *et al*. 2009) to select, for all the considered pairs of data and synthetics, the time windows within which the two traces have a reasonable agreement by imposing that criteria such as cross-correlation, amplitude ratio and time-shift satisfy goodness of fit requirements (i.e.: cross-correlation ≥ 0.7; |amplitude ratio| ≤ 1.3; |time-shift| ≤ 10 s). Full wave inversion could be strongly affected by inclusion of pulses poorly fitted by synthetic traces, leading to unstable solutions that map inaccuracies of the velocity model in the source moment tensor. Using FLEXWIN results in more stable solutions, reducing the inappropriate mapping effect. Therefore, the code CMT3D performs the moment tensor inversion considering only the selected windows for each pair of seismograms.

5 CMT3D RESULTS

In Section 5.1 we study the source parameters and behaviour of corresponding waveforms for the source solution obtained using CMT3D and 3-D MAMBo model, also in comparison to the TDMT+1D CIA solution. Then, we quantitatively study the source solution variability due to the sampling of the velocity model (Section 5.2) and to the azimuthal distribution of the stations (Section 5.3).

5.1 CMT solution and waveform analysis

Using the same 12 stations of Section 3.1, we invert again for moment tensor solution in order to study the effect of a 3-D structure and verify if the variability of inferred source parameters is caused by a poorly constrained velocity model. The resulting CMT3D + 3DMAMBo moment tensor solution has a VR equal to 56.1 per cent (green beachball in Fig. 2h). The goodness of the solution, quantified by a high VR, is reflected by the waveform fit (Fig. 3). Synthetics of the CMT3D + 3DMAMBo solution (green traces) match very well the observed seismograms both in amplitude and phase, not only for body waves but also in correspondence of the coda pulses. A good fit of later arrivals, often better than the TDMT+1DCIA case, is especially evident for both horizontal components (e.g. ROVR, SALO, MAIM and ASQU). Most of the synthetic traces of this solution needed to be shifted forward in time to maximize the correlation with data (i.e., almost all the time-shifts are positive). This could suggest that the wave speed model is generally too fast with respect to the real structure.

The resulting M_w and M_0 are 5.92 and 9.44e+24 dyne cm, respectively. This corresponds to a difference in M_w of 0.04 with respect to the TDMT+1DCIA solution. The chosen nodal plane is 44° south dipping, while strike and rake angles are, respectively, 96° and 82°, consistent with the kinematic of the area (Table 2).

For completeness, we have also tested the inversion for nine parameters, that is for depth, latitude and longitude as well, using CMT3D and MAMBo. The solution has $M_w = 5.95$, $M_0 = 1.06e+25$ dyne cm, strike/dip/rake = 93°/46°/78° and VR = 59.9 per cent. Moreover, the hypocentre becomes 561 m deeper, moves northward of 778 m and eastward of 2480 m. The solution is very similar to that obtained by inverting only for the six moment tensor components and the event location has small variations. Thus, in the following analysis, we have decided to invert only for six parameters and leave the study of hypocentre variability for future works.

Finally, to compare the 1-D and 3-D solutions and verify their compatibility, we apply an *a posteriori* FLEXWIN time window selection to synthetic waveforms and data of both cases. We thus construct the cumulative distributions in seconds of cross-correlation, amplitude ratio and time-shift values obtained for the two models (Fig. 6, see the caption for details). The distributions show that the CMT3D + 3DMAMBo solution has a larger total number of fitted seconds, that is it fits a larger portion of observed data. However, the behaviour of the two solutions is similar for high cross-correlation (Fig. 6a), low amplitude ratio (Fig. 6b) and low time-shift (Fig. 6c) values. This *a posteriori* analysis shows us that the two solutions are overall compatible.

5.2 Station selection effect

The results in Section 3.2 with the 1-D CIA model pointed out that a bootstrap analysis of the source solutions obtained by randomly selecting 12 stations out of the available 75 is significant to explore the effect of a given structure model on the estimate of source parameters. Thus, we perform the bootstrap calculation using the code CMT3D and the 3-D MAMBo model on the same 500 distributions of 12 stations adopted for the 1-D case. Empty green histograms in Fig. 4 are the distributions of the parameters obtained by considering all the 500 source inversions. Instead, the solid green histograms are constructed by discarding the 171 solutions with lower VR in order to obtain a total number of 3-D MAMBo solutions equal to the number of 1-D CIA solutions with VR > 30 per cent (329 solutions). In this way, the comparison of 1-D CIA and 3-D MAMBo histograms is statistically consistent since we are analysing the same number of samples.

The inferred median M_w value is 5.96 and the associated uncertainty, expressed as a confidence interval at 95 per cent, is [5.90–6.02]. Noteworthy, differently from what observed in the 1-D CIA analysis, the comparison between all the inversions and the ones with better VR (empty and solid histograms, respectively) highlights that the worst solutions obtained with 3-D MAMBo have high values of M_w. This result suggests that the highest

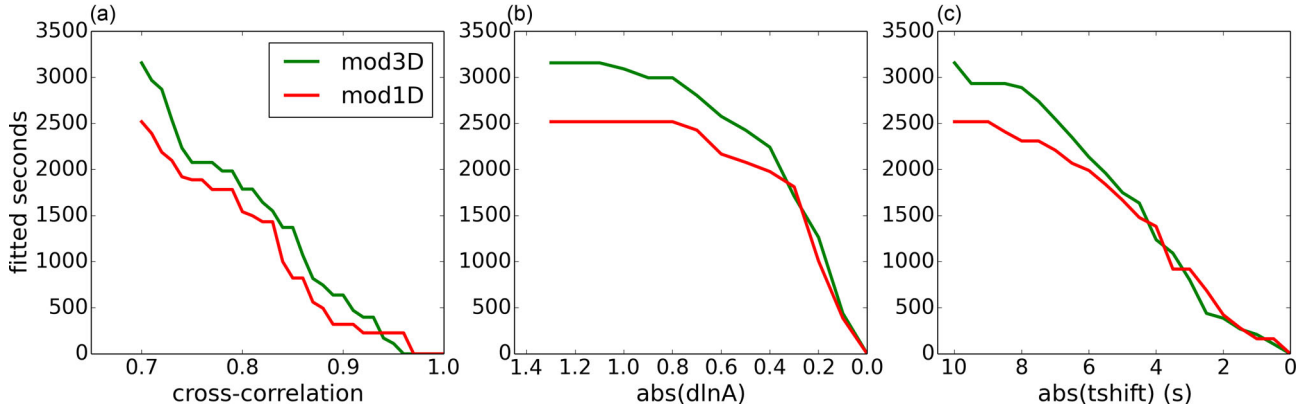

Figure 6. Misfit analysis for the TDMT+1DCIA (red) and CMT3D+3DMAMBo (green) MT solutions with 12 selected stations. The cumulative distributions represent the seconds of the data fitted by the synthetic traces as a function of the misfit criteria: (a) cross-correlation; (b) absolute value of the amplitude ratio $\mathrm{dln}A = \ln(A_{\mathrm{obs}}/A_{\mathrm{synt}})$, where A_{obs} is the amplitude of the observed trace in the selected window and A_{synt} the amplitude of the synthetic trace; (c) absolute value of the time-shift that quantifies the delay in time between observed and synthetic phase arrivals within the given window.

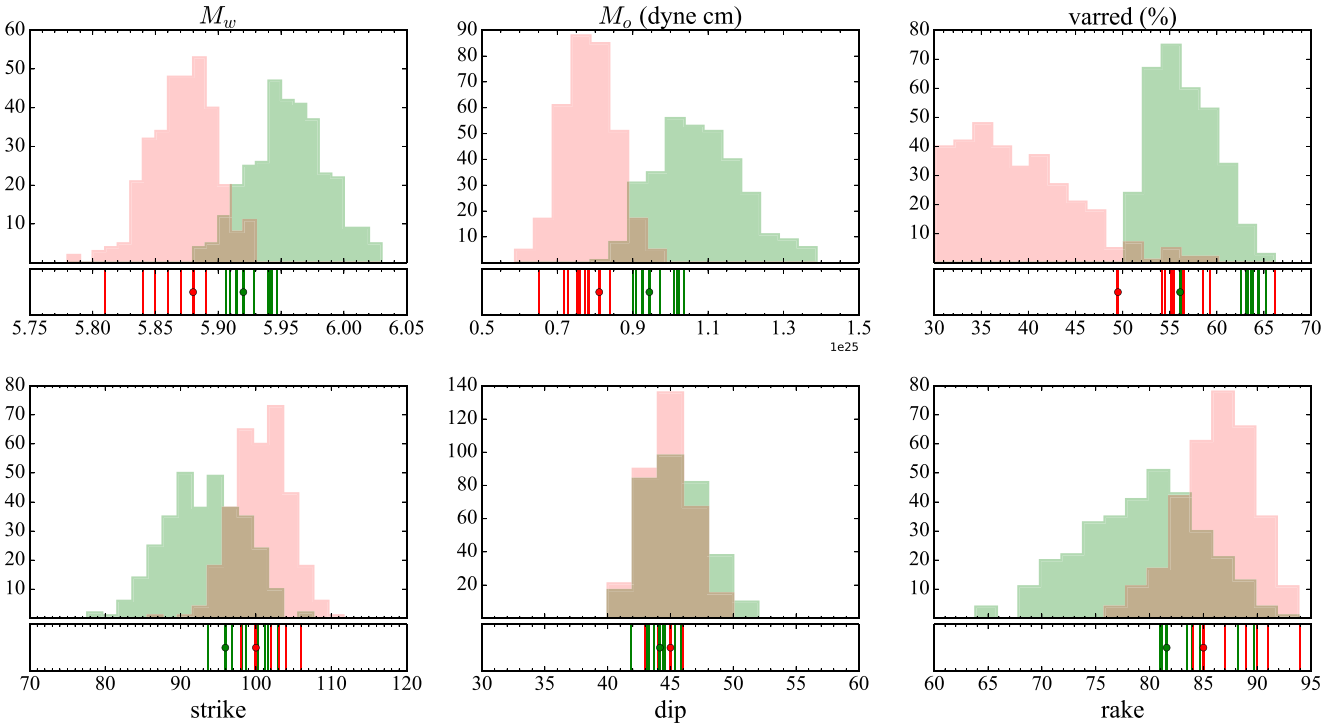

Figure 7. Histograms are the bootstrap distributions for the 1-D and 3-D 329 MT solutions as in Fig. 4. The thin solid lines in the boxes below each panel represent the 10 solutions, out of the 329, for the 1-D case in red and the 3-D case in green, with the highest values of the variance reduction VR. The solid lines with a middle dot in each box correspond to the source parameter values for the MT solutions calculated with 12 selected stations for the 1-D case in red (Section 3.1) and the 3-D case in green (Section 5.1).

VR solutions of both methodologies tend to reduce the plausible magnitude range. Hereinafter we focus only on the solid histograms.

Looking at Fig. 4, the discrepancy between the 1-D CIA and 3-D MAMBo distributions can be firstly attributed to the differences in the velocity models used in the inversion, that appear to be relevant already at our working frequencies. In particular, we note that especially for the dip, but also for strike and rake there is a good overlapping between the distributions for the 1-D CIA and 3-D MAMBo cases, while for M_w parameter the distributions are more separated although the overall variability, equal to 0.21 [5.81–6.02], is still lower than that observed in literature.

The distribution of VR values for the 3-D MAMBo solutions is narrower than that for the 1-D case and the values are generally larger. This result cannot be only attributable to the goodness of the 3-D model because in the latter methodology we perform the source inversions only on selected good time windows and not on the whole waveforms as in the TDMT procedure.

Contrary to the 1-D case, we note that the source parameter values for the CMT3D+3DMAMBo solution obtained with the 12 selected stations (green lines with a dot in Fig. 7) has an intermediate VR value (56.1 per cent) and the corresponding parameters are always located within the overlapping areas between the 1-D CIA and 3-D MAMBo distributions (Fig. 7).

A similar behaviour can be observed if we consider the 10 best solutions out of the 500 MT inversions for both 1-D CIA and 3-D MAMBo models (thin red and green lines in Fig. 7).

While the values of the parameters for the 10 best solutions of the 1-D case are pretty representative of the corresponding complete distributions, namely they already anticipate the uncertainty of the model, for the 3-D MAMBo case the parameters of the best solutions tend to cluster towards the overlapping areas. For strike, dip and rake distributions these areas are quite large resulting in best 3-D MAMBo solutions almost superimposed to best 1-D CIA solutions. This shows that the difference between the wave speed models has a weaker effect on the variability of the focal parameters than on the variability of M_w.

5.3 Station distribution effect

Following the analysis in Section 3.3, we then study the effect of the azimuthal distribution of the seismic stations on the variability of source solutions obtained with the 3-D MAMBo model.

Figs 5(b) and (c) show that, as for the 1-D case (Fig. 5a), the inversions present the lowest VR values when the stations on the Northern Apennines are included, that is for azimuth angles from $\sim$90° to $\sim$210°, while the best solutions are those for the north–northeast azimuth angles, although the sector from 30° to 90° includes a number of seismic stations that may be too low for a reliable estimate of the solution.

The VR values are in the range [33.8–73.9 per cent]. The variability range of M_w due to the station azimuth for the 3-D MAMBo case goes from 5.87 to 6.16, that is larger than the variability of the 1-D solutions and also larger than the variability resulting from the bootstrap analysis with MAMBo model (Fig. 4).

In particular, we observe that the worst 3-D MAMBo source solutions have the highest values of M_w (as previously already highlighted in Fig. 4). This suggests that for the stations in these azimuths the 3-D MAMBo model is missing features to match the amplitude of the observed data (Molinari *et al*. 2015). Nevertheless, even if the source inversion tries to compensate by increasing the magnitude, the resulting synthetics for stations on the Apennines still have a poor fit of the data.

6 QUANTITATIVE MOMENT TENSOR COMPARISON

In order to investigate the kinematic behaviour suggested by the obtained moment tensors (both 1-D and 3-D solutions) and to measure the difference among the solutions, we adopt the distance parameter proposed by Tape & Tape (2012). The distance between two full moment tensors M and N, d_{MN}, is defined as:

$$d_{MN} = \frac{1}{2}\left(1 - \frac{\sum m_{ij} n_{ij}}{\sqrt{m_{ij}^2}\sqrt{n_{ij}^2}}\right), \quad (2)$$

where the summation is over both indices of tensor components m_{ij} and n_{ij}. We calculate the distance between all the 329 MT solutions coming from the bootstrap analysis for both the 1-D and 3-D cases and we get the multivariate geometric median defined as the point P in the tensor space Ω that minimizes D, that is the sum of the distances of a distribution of tensors Δ:

$$D(P) = \min \sum_{i\in\Omega}^{j\in\Delta} d_{ij}. \quad (3)$$

The beachballs in Figs 8(a) and (b) are our final moment tensor solutions for the main shock of the Emilia sequence obtained by superimposing, for the two considered wave speed models, the computed multivariate geometric medians (red for 1-D CIA, green for 3-D MAMBo) and the 329 moment tensor solutions (in black). The values of the nodal plane corresponding to the double-couple mechanism closest to the geometric median solution are 101°/44°/87° for strike/dip/rake of the 1-D case and 93°/45°/79° for the 3-D case (Table 3). From Fig. 8(c), we observe that the 1-D CIA case shows a lower variability in moment tensor components with respect to the 3-D case. Nevertheless, in both cases, the values of d_{MN} range between 0 and 0.045. Moreover, the resulting distance between the 1-D and 3-D geometric medians is 0.008, stating the kinematic equivalence of the two final solutions. The lower variability for the 1-D CIA is evident also in Fig. 9 where we visualize the multivariate kernel density estimation (kde) for 1-D and 3-D bootstrap distributions of nodal plane orientation of the corresponding closest double-couple mechanisms, evaluated with the Parzen-window method (Parzen 1962). We immediately note that strike and rake are strongly correlated, as also stated by the correlation matrix (see additional material Fig. S3). The uncertainty on the focal parameters is then calculated by the marginal histograms of the multivariate kde along strike, dip and rake and considering the confidence interval at 95 per cent (see values in Table 3). A more rigorous approach would have involved the analysis of a multivariate joint distribution of the 6 independent components of the moment tensor (Valentine & Trampert 2012). Such distribution is difficult to be visualized and, in this case, it does not provide additional information compared to the more friendly approach of the nodal planes. Nevertheless, for sake of clarity, in the additional material we visualize the 6-D distributions as marginal histograms (Fig. S4) and corresponding correlation matrixes (Fig. S5).

As a final remark, we propose some considerations about the null space and our capability to explore the full variability of the solutions. Concerning the mechanism of this event, we highlight that the kinematic source parameters are acceptably stable across several approaches, including SAR and GPS inversion or local exploration seismology (i.e. Vannoli *et al*. 2015 for review). The importance of the null space is also reduced by geological knowledge, that provides some *a priori* information, constraining strike and rake directions.

7 CONCLUSIONS

The main goal of this work is to estimate the earthquake source parameters and the associated uncertainties for the 2012 May 20 Emilia main shock by exploring suitable moment tensor inversion methodologies, available velocity models and the effect of station distribution. This allows us to release a better constrained moment tensor and unravel the variability issue due to the inaccuracies affecting this earthquake source solution.

We firstly investigate the effect of the velocity model (Sections 3.1 and 5.1). By choosing a particular distribution of 12 stations with good azimuth coverage and adopting 6 different velocity models and two inversion techniques, we obtain moment tensor solutions characterized by a VR ranging from less than 30 per cent (not-confident solutions) to 56 per cent, highlighting that the moment tensor solutions match differently the complexity of the seismograms.

Among the five different 1-D models we have tested, CIA comes out to be the one that gives the best results, as shown in Table 2. The obtained high VR (49.5 per cent) demonstrates that, even without accounting for slow sedimentary layers, at this frequency and magnitude, this model satisfactorily reproduces the waveforms excited by the main shock. Differently, PADANIA and VENETIAN

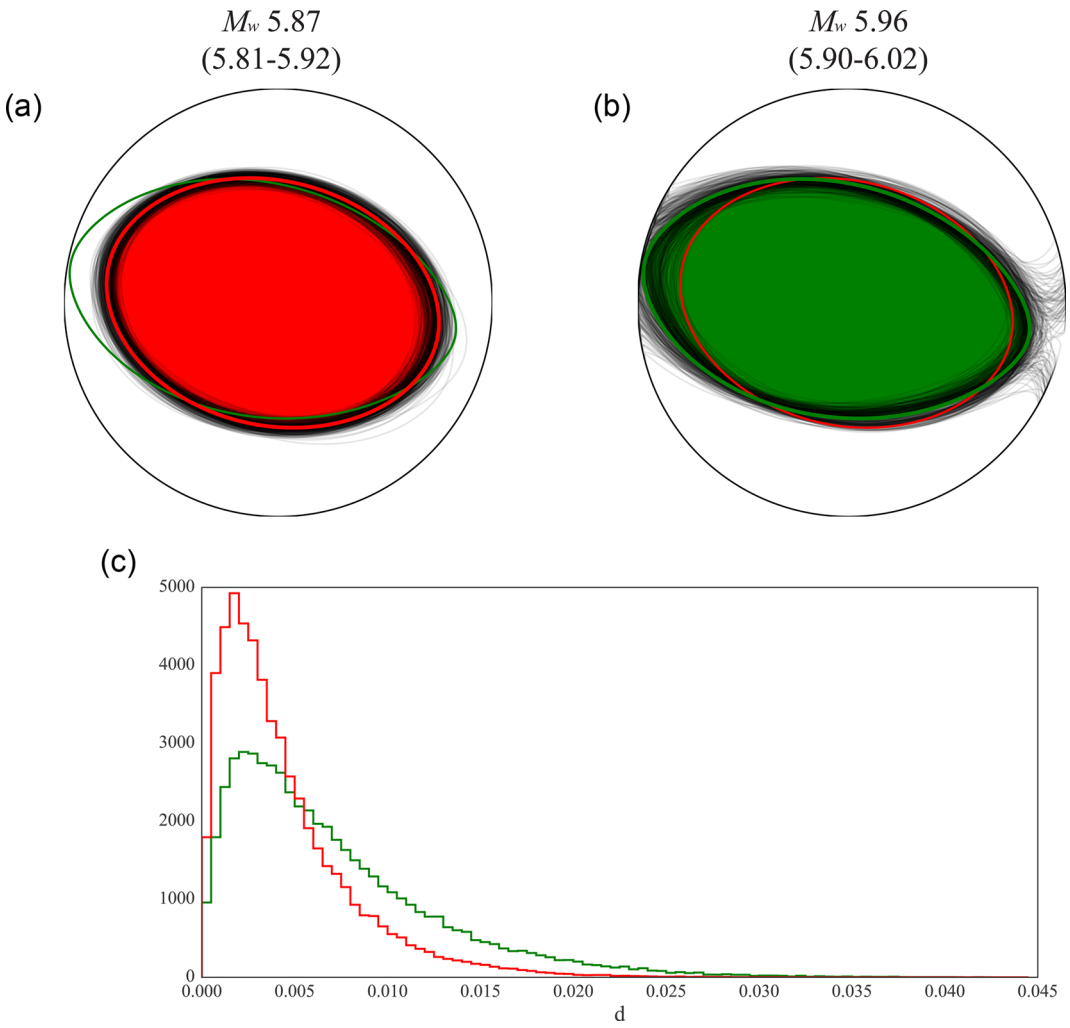

Figure 8. Results for the focal mechanism parameters of the Emilia main shock from the MT inversion with (a) the 1-D CIA and (b) the 3-D MAMBo models. The beachballs for the two cases are constructed by superimposing the mechanisms corresponding to the best 329 bootstrap solutions (in black) and the geometric median of the focal mechanism (1-D CIA in red, 3-D MAMBo in green in panels (a) and (b), respectively) resulting from the multivariate analysis of strike, dip and rake. For comparison, in panel (a) we add the median solution of the 3-D focal mechanism as a thin green ellipse, while in panel (b) we add the median solution of the 1-D focal mechanism as a thin red ellipse. The numbers on the top of the beachballs indicate the medians and the uncertainties for M_w. Panel (c) shows the distance d_{ij}, respectively for moment tensors of 1-D CIA (red) and 3-D MAMBo (green) bootstrap distributions.

PLAIN, characterized by very low V_S velocity in the first 2–3 km, introduce complexities not existing in the real data, therefore we are not confident in the resulting M_w estimates. Our results criticize the idea that adopting very local velocity profiles to represent a large and heterogeneous region improves the reliability of moment tensor solutions. The last two 1-D models, PREM and IASP91, have been evaluated to verify their aptitude for generating the highest magnitudes found in literature. The resulting M_w values (5.91 and 5.96) are the highest among the tested 1-D models, but in the chosen frequency range they do not reach the literature results. In our simulations, these global models reproduce the amplitude of the main body waves and do not generate fake later arrivals. However, they are too fast to allow a good time alignment between real and synthetic phases. Finally, the use of the 3-D MAMBo wave speed model, in which the sediment layers exist and are carefully constrained, provides a source solution that shows a better fit of the observed data for many of the considered stations, especially for later arrivals. Table 2 summarizes the results for these six wave speed models. These solutions show an overall variability of 0.35 units in the estimate of moment magnitude, while strike, dip and rake have variations less than 10°: this is the difference effectively coming from the velocity model. In general, our results show that a well calibrated 1-D model is able to reproduce the main features of the earthquake source.

In order to quantify the M_w estimates' uncertainty, we perform a bootstrap analysis by using 1-D CIA and 3-D MAMBo models. The results of this analysis can be outlined considering for each methodology the M_w median value of the resulting distribution (Fig. 4), which is 5.87 for 1-D CIA case and 5.96 for 3-D MAMBo case. The difference between the two medians (0.09) is very much lower than the variability between the solutions reported in literature and absolutely acceptable from a seismological point of view. The associated uncertainty can be then estimated from the corresponding distributions as the confidence interval at 95 per cent. The results are [5.81–5.92] for 1-D CIA case and [5.90–6.02] for 3-D MAMBo case. These analyses document that using our 3-D model corroborates the magnitude obtained with the best 1-D model but, for the studied earthquake, it is not a decisive choice since the frequencies inverted for events with $M_w > 5.5$ do not sample efficaciously the details of the models. If higher frequencies are demanded, for

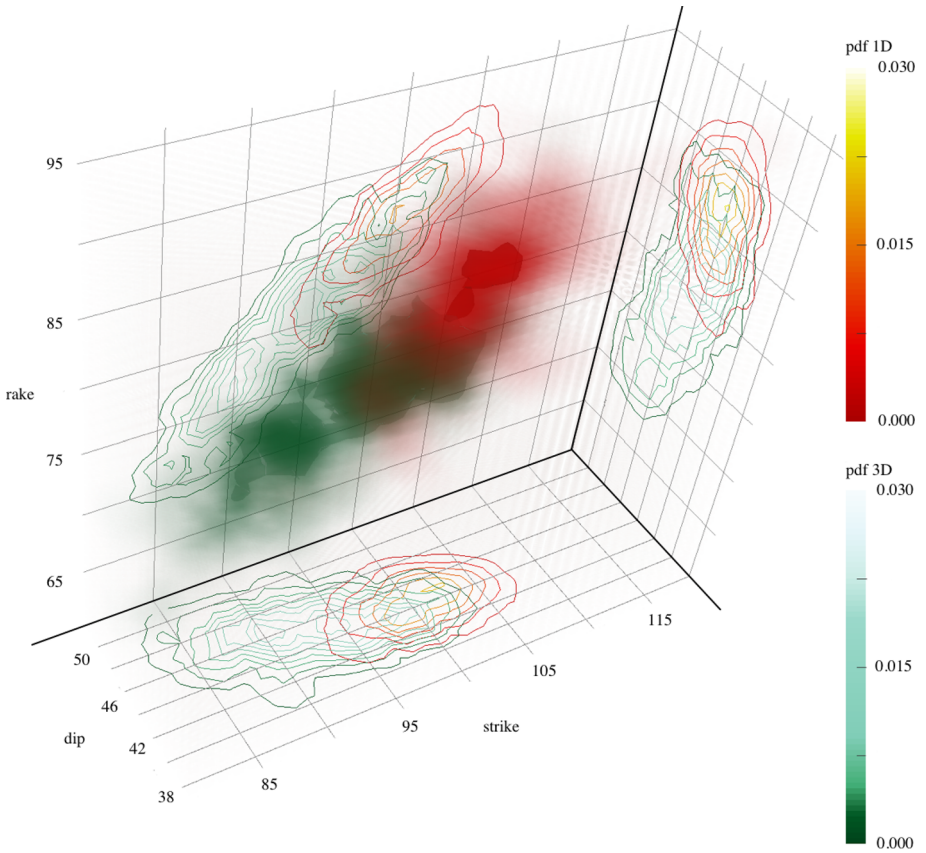

Figure 9. Multivariate kernel density estimation (kde) for the bootstrap distributions of nodal plane orientation for 1-D CIA (red scale) and 3-D MAMBo (green scale) MT solutions, evaluated with the Parzen-window method (Parzen 1962). On the axial planes, we illustrate the 2-D marginal view of these joint kde. The correlation matrixes are reported in the additional material (Fig. S3).

example to calculate moment tensor solutions for smaller earthquakes, sediment layers have to be included thus a full 3-D model is required.

Performing the bootstrap analysis allows us to estimate the uncertainty of the moment tensor solutions due to the station selection procedure and the approximated sampling of the Earth by a given wave speed model. Moreover, we highlight that the 3-D best solutions cluster within the overlapping areas of the 1-D and 3-D bootstrap distributions. This evidence supports the hypothesis that the solutions provided by 1-D CIA and 3-D MAMBo models are part of a more general distribution that accounts not only for the internal source parameter uncertainty but also for the variability related to the choice of wave speed model. Our two velocity models do not explore thoroughly the model space, but we could expect that, if in the future more refined 3-D velocity models were available (e.g. with better sampling of the Northern Apennines), they will give source parameter values that lie in the confidence intervals of these two best models.

In this study, we also investigate the effect of the heterogeneous crustal structure on the moment tensor solutions due to the distribution of selected stations. The variability range of M_w due to the station azimuth for the 1-D case is 0.16 while is 0.29 for the 3-D model. In both cases the inversions present the lowest VR values when the stations on the Northern Apennines are included, while the best solutions are those for the north–northeast azimuth angles. The variability range of M_w results always larger than the variability resulting from the bootstrap analysis. This suggests that solutions obtained with large azimuthal gaps could only contain limited features of structure and source, as much as the velocity model diverges from the real crustal structure. We are aware that point source approximation shows azimuth dependence due to source radiation and could also have directivity effects at low frequencies. However, the moderate size of this earthquake, the analysed frequency range and the distance of the selected stations prevent this condition. We thus remark that the MT inversion process is sensitive to choices made on the data set and approximation of adopted Earth model that are the main sources of uncertainty in the moment tensor solution. To obtain reliable source parameters (and therefore accurate hazard information) it is thus essential to have good-quality models of Earth structure for the region and frequency band.

We additionally perform a quantitative analysis of the kinematical behaviours by computing the distance between the 329 best MT solutions, both 1-D and 3-D, and deriving the multivariate geometric medians. Our 1-D CIA and 3-D MAMBo final solutions manifest distance $d = 0.008$, demonstrating that the two MTs have a comparable behaviour and can be both considered seismologically well constrained. Finally, the values of our preferred nodal planes for the 2012 May 20 main shock are: 101°/44°/87° for strike/dip/rake of the 1-D case and 93°/45°/79° for the 3-D case.

It is possible that the considered case study is particularly extreme due to the strong heterogeneities of the sedimentary layers of the Po Plain. Nevertheless, its peculiarity allows us to highlight how the moment magnitude, usually considered a stable parameter, could be seriously affected by the unsupported starting choices, as uncalibrated velocity models, unbalanced station distributions

and explored frequency ranges. We believe that the combination of these factors is the main cause of the large variability on moment magnitude found in literature.

Considering the present study, we endorse that, where self-consistency is crucially important, a full control on the variability of the moment tensor source parameters is essential. The moment tensor uncertainties are rarely shown in literature, instead such information is pivotal for researchers that plan to adopt published seismic moment for inferences outside the scope and the assumptions of the solution itself. For these reasons, we suggest that the seismic moment solutions should be released in a reproducible framework characterized by disclosed wave speed models and explicit processing workflows. It should also include, for moderate-to-large earthquakes, an analysis of the estimates' uncertainty, including, when it is possible, the impact of the choice of the velocity model. The provenances, indeed, should represent an intrinsic component of moment tensor catalogues.

ACKNOWLEDGEMENTS

TDMT-code, used to compute moment tensor with 1-D velocity models, could be downloaded here: ftp://www.orfeus-eu.org/pub/software/iaspei2003/8511.html. CMT3D-code, used to compute moment tensor solution in 3-D velocity model, could be downloaded here: https://github.com/QuLogic/GRD_CMT3D. Moment Tensors in Figs 2(c)–(g) are plotted with MoPaD (Krieger & Heimann 2012). Figs 2(a) and (b) are made using the Generic Mapping Tools version 4.2.1 (http://www.soest.hawaii.edu/gmt). Fig. 3 is obtained with SAC Tool (http://www.iris.edu/dms/nodes/dmc/software/downloads/sac/) and ObsPy (The ObsPy Development Team 2015). Figs 4–8, S1, S2, S4 are created using Matplotlib 1.4.3 (Hunter 2007). Figs S3 and S5 are created using Seaborn 0.6.0 (Waskom *et al*. 2015). Fig. 9 is created using Paraview 4.4 (Ayachit 2015). The authors would like to thank Anna Maria Lombardi, Warner Marzocchi and Carl Tape for the helpful discussions. We are also grateful to the editor, Ingo Grevemeyer, and to Andrew Valentine and an anonymous reviewer for their comments and suggestions. This research has been supported by Project TRAMONTO, INGV Struttura Terremoti.

REFERENCES

Ayachit, U., 2015. *The ParaView Guide: A Parallel Visualization Application,* Kitware.

Cesca, S., Braun, T., Maccaferri, F., Passarelli, L., Rivalta, E. & Dahm, T., 2013. Source modelling of the M5-6 Emilia-Romagna, Italy, earthquakes, (2012 May 20–29), *Geophys. J. Int.,* **193,** 1658–1672.

Dreger, D.S. & Helmberger, D.V., 1993. Determination of source parameters at regional distances with 3-component sparse network data, *J. geophys. Res.,* **98,** 8107–8125.

Dziewonski, A.M. & Anderson, D.L., 1981. Preliminary reference Earth model, *Phys. Earth planet. Inter.,* **25,** 297–356.

Ekström, G., Nettles, M. & Dziewonski, A.M., 2012. The global CMT project 2004–2010: centroid-moment tensors for 13 017 earthquakes, *Phys. Earth planet. Inter.,* **200–201,** 1–9.

Gasperini, P., Lolli, B., Vannucci, G. & Boschi, E., 2012. A comparison of moment magnitudes estimates for the European-Mediterranean and Italian regions, *Geophys. J. Int.,* **190,** 1733–1745.

Herrmann, R.B., Malagnini, L. & Munafò, I., 2011. Regional moment tensor of the 2009 L'Aquila earthquake sequence, *Bull. seism. Soc. Am.,* **101**(3), 975–993.

Hjörleifsdóttir, V. & Ekström, G., 2010. Effects of three-dimensional Earth structure on CMT earthquake parameters, *Phys. Earth planet. Inter.,* **179,** 178–190.

Hunter, J.D., 2007. Matplotlib is a 2D graphics package used for Python for application development, interactive scripting, and publication-quality image generation across user interfaces and operating systems, *Comput. Sci. Eng.,* **9**(3), 90–95.

Kennett, B.L.N. & Engdahl, E.R., 1991. Traveltimes for global earthquake location and phase identification, *Geophys. J. Int.,* **122,** 429–465.

Krieger, L. & Heimann, S., 2012. MoPaD - moment tensor plotting and decomposition: a tool for graphical and numerical analysis of seismic moment tensors, *Seismol. Res. Lett.,* **83**(3), 589–595.

Kubo, A., Fukuyama, E., Kawai, H. & Nonomura, K., 2002. NIED seismic moment tensor catalogue for regional earthquakes around Japan: quality test and application, *Tectonophysics,* **356,** 23–48.

La Longa, F., Crescimbene, M. & Camassi, R., 2014. Il contrasto di voci e dicerie sui terremoti del 20 e 29 Maggio 2012 in Pianura Padana, GNGTS, Available at: http://hdl.handle.net/2122/9246.

Liu, Q., Polet, J., Komatitsch, D. & Tromp, J., 2004. Spectral-element moment tensor inversions for earthquakes in Southern California, *Bull. seism. Soc. Am.,* **94**(5), 1748–1761.

Maggi, A., Tape, C., Chen, M., Chao, D. & Tromp, J., 2009. An automated time window selection algorithm for seismic tomography, *Geophys. J. Int.,* **178,** 257–281.

Magnoni, F., 2012. Spectral-element and adjoint 3D full-wave tomography for the lithosphere of central italy, *PhD thesis,* Dep. of Geophys., Università di Bologna Alma Mater Studiorum, Bologna, Italy, doi:10.6092/unibo/amsdottorato/4275.

Malagnini, L., Herrmann, R.B., Munafò, I., Buttinelli, M., Anselmi, M., Akinci, A. & Boschi, E., 2012. The 2012 Ferrara seismic sequence: regional crustal structure, earthquake sources, and seismic hazard, *Geophys. Res. Lett.,* **30,** L19302, doi:10.1029/2012GL053214.

Marzocchi, W., Lombardi, A.M. & Casarotti, E., 2014. The establishment of an operational earthquake forecasting system in Italy, *Seism. Res. Lett.,* **85**(5), 961–969.

Meletti, C., D'Amico, V., Ameri, G., Rovida, A. & Stucchi, M., 2012. Seismic hazard in the Po Plain and the 2012 Emilia earthquakes, *Ann. Geophys.,* **55**(4), doi:10.4401/ag-6158.

Molinari, I., Argnani, A., Morelli, A. & Basini, P., 2015. Development and testing of a 3D seismic velocity model of the Po Plain sedimentary basin, Italy, *Bull. seism. Soc. Am.,* **105**(2a), doi:10.1785/0120140204.

Morelli, A. & Dziewonski, A.M., 1991. Joint determination of lateral heterogeneity and earthquake location, in *Glacial Isostasy, Sea-Level and Mantle Rheology,* pp. 515–534, eds Sabadini, R., Lambert, K. & Boschi, E., Kluwer.

Parzen, E., 1962. On the estimation of a probability density function and the mode, *Ann. Math. Stats.,* **33,** 1065–1076.

Pavlis, G.L. & Booker, J.R., 1980. The mixed discrete-continuous inverse problem: application to the simultaneous determination of earthquake hypocenters and velocity structure, *J. geophys. Res.,* **85,** 4801–4810.

Peter, D. *et al.*, 2011. Forward and adjoint simulations of seismic wave propagation on fully unstructured hexahedral meshes, *Geophys. J. Int.,* **186,** 721–739.

Pondrelli, S., Salimbeni, S., Morelli, A., Ekstrom, G., Postpischl, L., Vannucci, G. & Boschi, E., 2011. European-mediterranean regional centroid moment tensor catalog: solutions for 2005–2008, *Phys. Earth planet. Inter.,* **185,** 74–81.

Pondrelli, S., Salimbeni, S., Perfetti, P. & Danecek, P., 2012. Quick regional centroid moment tensor solutions for the Emilia 2012 (northern Italy) seismic sequence, *Ann. Geophys.,* **55**(4), 615–621.

Saikia, C.K., 1994. Modified frequency wave-number algorithm for regional seismograms using Filon's quadrature: modeling of Lg waves in eastern North America, *Geophys. J. Int.,* **118,** 142–158.

Saraò, A. & Peruzza, L., 2012. Fault-plane solutions from moment-tensor inversion and preliminary Coulomb stress analysis for the Emilia Plain, *Ann. Geophys.,* **55**(4), 647–654.

Scognamiglio, L., Tinti, E. & Michelini, A., 2009. Real-time determination of seismic moment tensor for Italian Region, *Bull. seism. Soc. Am.,* **99**(4), 2223–2242.

Scognamiglio, L. *et al.*, 2012. The 2012 Pianura Padana Emiliana seismic sequence: locations, moment tensors and magnitudes, *Ann. Geophys.,* **55,** 4, doi:10.4401/ag-6159.

Šílený, J., 2004. Regional moment tensor uncertainty due to mismodeling of the crust, *Tectonophysics,* **383**(3–4), 133–147.

Stucchi, M., Meletti, C., Montaldo, V., Crowley, H., Calvi, G.M. & Boschi, E., 2011. Seismic hazard assessment (2003–2009) for the Italian Building Code, *Bull. seism. Soc. Am.,* **101,** 1885–1911.

Tape, W. & Tape, C., 2012. Angle between principal axis triples, *Geophys. J. Int.,* **191,** 813–831.

The ObsPy Development Team, 2015. ObsPy 0.10.2, doi:10.5281/zenodo.17641.

Valentine, A.P. & Trampert, J., 2012. Assessing the uncertainties on seismic source parameters: towards realistic error estimates for centroid-moment-tensor determinations, *Phys. Earth planet. Inter.,* **210–211,** 36–49.

Valentine, A.P. & Woodhouse, J.H., 2010. Reducing errors in seismic tomography: combined inversion for sources and structure, *Geophys. J. Int.,* **180,** 847–857.

Vannoli, P., Burrato, P. & Valensise, G., 2015. The Seismotectonics of the Po Plain (Northern Italy): tectonic diversity in a blind faulting domain, *Pure appl. Geophys.,* **172**(5), 1105–1142.

Vuan, A., Klin, P., Laurenzano, G. & Priolo, E., 2011. Far-source long-period displacement response spectra in the Po and Venetian Plains (Italy) from 3D wavefield simulations, *Bull. seism. Soc. Am.,* **101**(3), 1055–1072.

Wald, D.J., Quitoriano, V., Heaton, T.H., Kanamori, H., Scrivner, C.W. & Worden, C.B., 1999. TriNet "ShakeMaps": rapid generation of peak ground motion and intensity maps for earthquakes in Southern California, *Earthq. Spect.,* **15**(3), 537–555.

Waskom, M. *et al.*, 2015. Seaborn: v0.6.0 (June 2015), doi:10.5281/zenodo.19108.

Werner, M.J. & Sornette, D., 2008. Magnitude uncertainties impact seismic rate estimates, forecasts, and predictability experiments, *J. geophys. Res.,* **113,** B08302, doi:10.1029/2007JB005427.

SUPPORTING INFORMATION

Additional Supporting Information may be found in the online version of this paper:

Figure S1. Results from the bootstrap analysis with 24 randomly chosen stations. Empty histograms represent the source parameters resulting from all the 500 MT solutions, red is for 1-D inversion with CIA velocity model, green is for 3-D inversion with MAMBo model. Solid red histograms are the 1-D MT solutions with VR > 30 per cent. Solid green histograms are the corresponding best MT solutions obtained with 3-D model. Red and green solid lines in M_w and M_0 panels are the medians calculated for the distributions of the best MT solutions of 1-D and 3-D cases, respectively.

Figure S2. Histograms as in Fig. S1 for a bootstrap analysis with 36 randomly chosen stations.

Figure S3. Nodal plane orientation correlation matrix for the bootstrap distributions of the double-couple mechanisms closest to the 329 best MT solutions of 1-D CIA (left) and 3-D MAMBo (right).

Figure S4. Marginal histograms for the six moment tensor components obtained from the 6-D distribution of the moment tensor. Colours and solid/empty style of the histograms are as in Fig. S1.

Figure S5. Moment tensor component correlation matrix of the bootstrap distributions of the 329 best MT solutions for 1-D CIA (left) and 3-D MAMBo (right).

(http://gji.oxfordjournals.org/lookup/suppl/doi:10.1093/gji/ggw173/-/DC1).

Please note: Oxford University Press is not responsible for the content or functionality of any supporting materials supplied by the authors. Any queries (other than missing material) should be directed to the corresponding author for the paper.

SUPPLEMENTARY MATERIAL

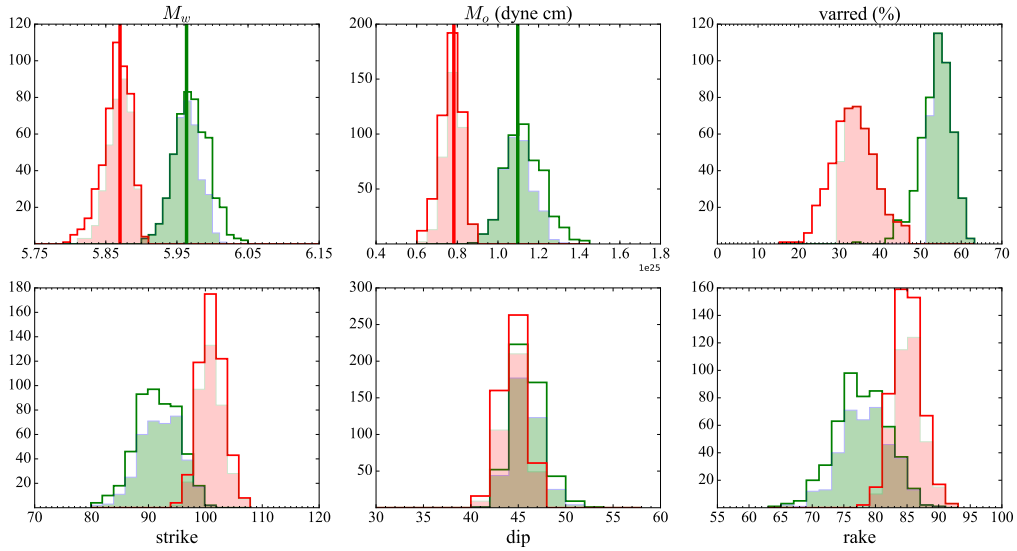

A1. Results from the bootstrap analysis with 24 randomly chosen stations. Empty histograms represent the source parameter resulting from all the 500 MT solutions, red is for 1D inversion with CIA velocity model, green is for 3D inversion with MAMBo model. Solid red histograms are the 1D MT solutions with VR > 30%. Solid green histograms are the corresponding best MT solutions obtained with 3D model. Red and green solid lines in M_w and M_0 panels are the medians calculated for the distributions of the best MT solutions of 1D and 3D cases respectively.

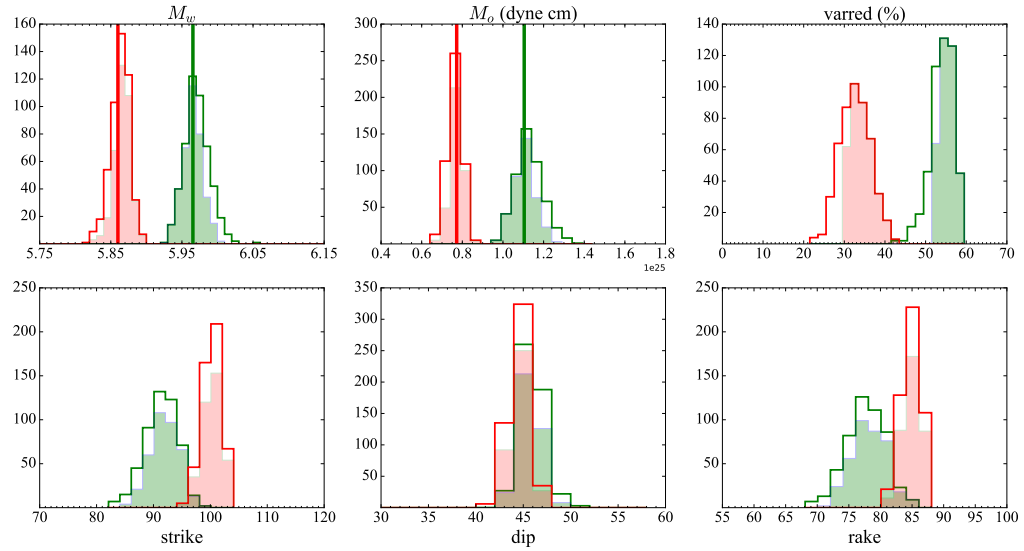

A2. Histograms as in Figure A1 for a bootstrap analysis with 36 randomly chosen stations.

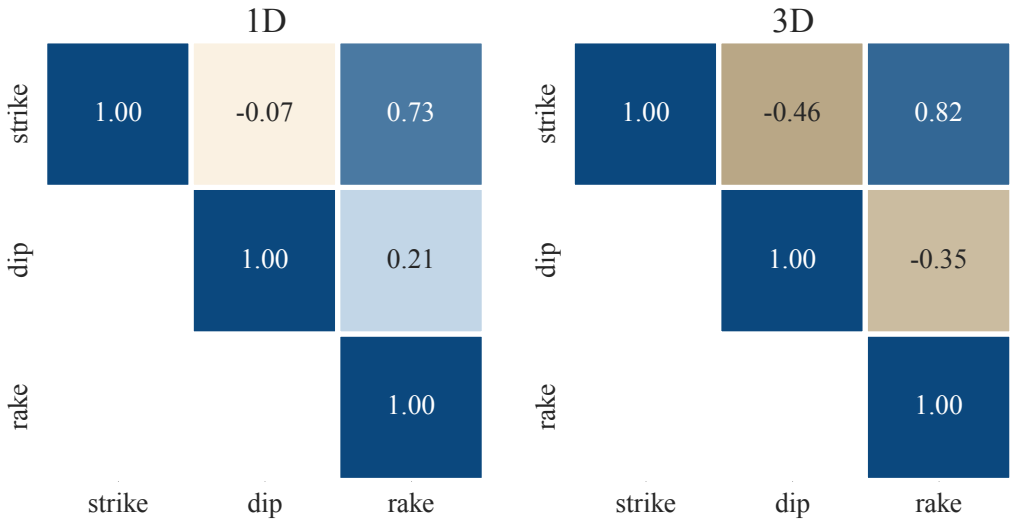

A3. Nodal plane orientation correlation matrix for the bootstrap distributions of the double-couple mechanisms closest to the 329 best MT solutions of 1D CIA (left) and 3D MAMBo (right).

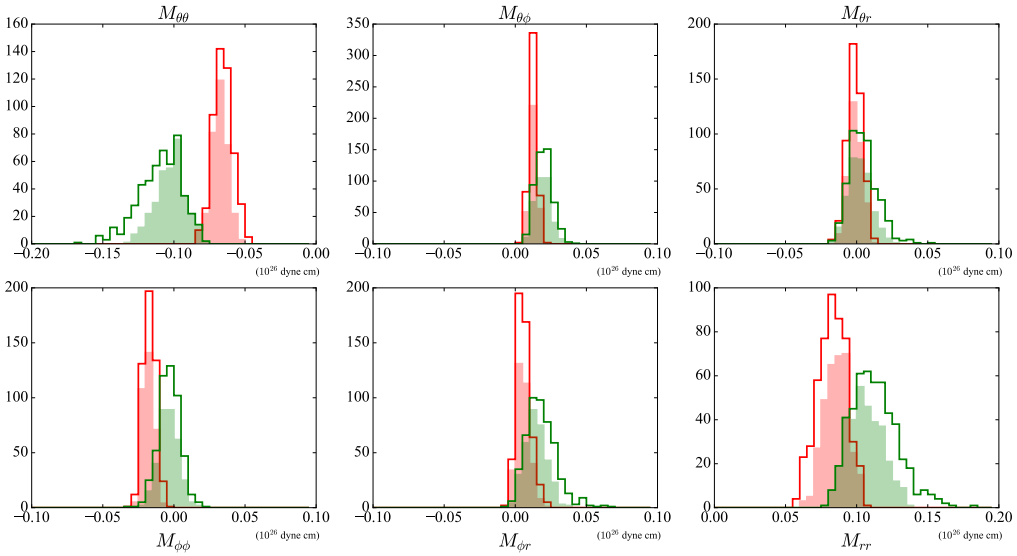

A4. Marginal histograms for the 6 moment tensor components obtained from the 6 dimensional distribution of the moment tensor. Colours and solid/empty style of the histograms are as in Figure A1.

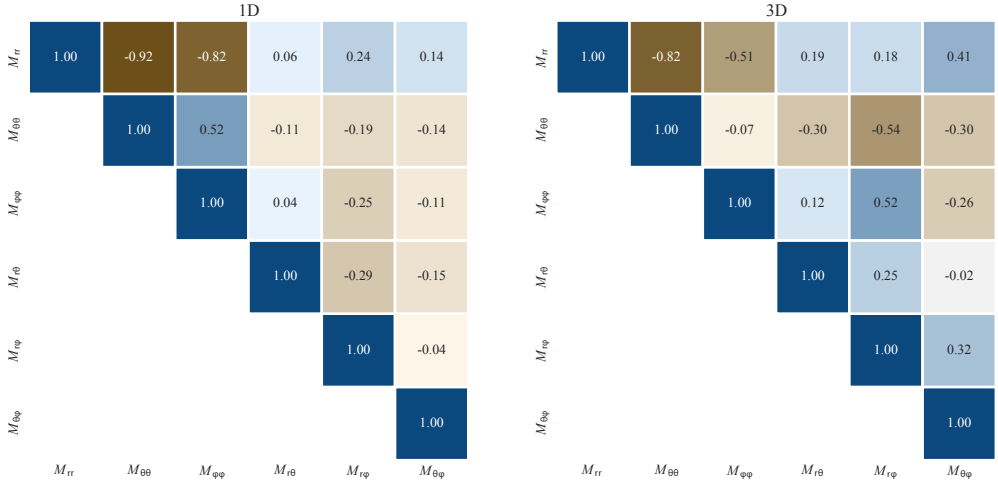

A5. Moment tensor component correlation matrix of the bootstrap distributions of the 329 best MT solutions for 1D CIA (left) and 3D MAMBo (right).